Msweli, Nondumiso Prudence; Akinwamide, Samuel Olukayode; Olubambi, Peter Apata; Obadele, Babatunde Abiodun

**Microstructure and biocorrosion studies of spark plasma sintered yttria stabilized zirconia reinforced Ti6Al7Nb alloy in Hanks' solution**

*Published in:*
Materials Chemistry and Physics

*DOI:*
10.1016/j.matchemphys.2022.126940

Published: 19/10/2023

*Document Version*
Publisher's PDF, also known as Version of record

Materials Chemistry and Physics 293 (2023) 126940

Contents lists available at ScienceDirect

Materials Chemistry and Physics

journal homepage: www.elsevier.com/locate/matchemphys

# Microstructure and biocorrosion studies of spark plasma sintered yttria stabilized zirconia reinforced Ti6Al7Nb alloy in Hanks' solution

Nondumiso Prudence Msweli [a], Samuel Olukayode Akinwamide [a,b,*], Peter Apata Olubambi [a], Babatunde Abiodun Obadele [a,c]

[a] *Centre for Nanomechanics and Tribocorrosion, School of Chemical, Mining and Metallurgy, University of Johannesburg, South Africa*
[b] *Centre for Advanced Manufacturing and Materials, Department of Mechanical Engineering, Aalto University, Espoo, Finland*
[c] *Department of Chemical, Materials and Metallurgical Engineering, Bostwana International University of Science and Technology, Palapye, Botswana*

## HIGHLIGHTS

- Ti6Al7Nb shows a two-phase microstructure with increased grains.
- The addition of YSZ reinforcements reveals the presence of evenly distributed α+β lamellae.
- Enhanced hardness property of reinforced titanium composites is ascribed to solid solution strengthening.
- A significant noble shift in $E_{corr}$ and reduces the corrosion current density is evident in the titanium composites.

## ARTICLE INFO

*Keywords:*
Ti6Al7Nb
Yttria stabilized zirconia
Biomedical
Potentiodynamic polarization
Dental implant

## ABSTRACT

A study of spark plasma sintered Ti6Al7Nb alloy reinforced with yttria stabilized zirconia (YSZ) has been carried out to assess the biocorrosion response in Hank's solution. The results indicate that the microstructural changes resulting from YSZ addition to Ti6Al7Nb were considerably different from pure Ti6Al7Nb. All the Ti6Al7Nb + YSZ composites showed a higher Vickers microhardness value with Ti6Al7Nb + 10%YSZ exhibiting the most enhanced hardness value of 955.3 $HV_{0.1}$. Furthermore, all Ti6Al7Nb + YSZ present higher corrosion resistance in Hank's solution than Ti6Al7Nb alloy except Ti6Al7Nb + 1YSZ which shows a significant drop in $E_{corr}$ and $I_{corr}$ values. This could be due to grain refinement with less stable oxide film growth kinetics. The combination of mechanical property and corrosion resistance of the fabricated Ti6Al7Nb + YSZ alloy could make it a suitable material for dental implant in the nearest future.

## 1. Introduction

There has been a sporadic increase in patients requiring biomedical implants/surgery with artificial alternatives. Such implants include but are not limited to maxillofacial [1], prostheses [2], hip joint [3], and dental implants [4]. The price of the latter costs between $1500 and $2000 per implant. Also, the failure rate of dental implants has been estimated to be about 5–10% either shortly or years later [5]. Consequence upon these dental implant statistics, in-depth research on the fabrication of biomaterials that are suitable for dental implants has been of keen interest in materials and biomedical engineering. A major factor that should be considered is the biocompatibility of the implant material in the oral cavity. Metallic biomaterials are suitable for load-bearing applications; hence, they should have sufficient fatigue strength and appreciable hardness. Metallic materials are preferably used in comparison to polymeric and ceramic materials, owing to advanced manufacturing technologies whose parameters can be optimized to achieve improved properties. Although austenitic stainless steel [6] and Co–Cr–Mo [7] alloys have been reportedly used for the fabrication of dental implant biomaterials, however, titanium alloys have proven to be more advanced and attractive for dental and other biomedical applications.

Pure titanium and Ti6Al4V alloys have been widely used in the biomedical industry even though they were originally designed as structural materials for automobile and aerospace applications [8,9]. Moreover, Ti6Al4V alloy is characterized by the low elastic modulus,

* Corresponding author. Advanced Manufacturing and Materials Research Group, Department of Mechanical Engineering, Aalto University, Finland.
*E-mail addresses:* akinwamidekayode@gmail.com, samuel.akinwamide@aalto.fi (S.O. Akinwamide).

https://doi.org/10.1016/j.matchemphys.2022.126940
Received 19 August 2022; Received in revised form 20 October 2022; Accepted 20 October 2022
Available online 25 October 2022

**Table 1**
Chemical composition of Ti6Al7Nb and YSZ powders.

| Elements (mass %) | Ti | Al | Nb | C | Fe | O | N | Zr | Y | Hf | Na | O |
|---|---|---|---|---|---|---|---|---|---|---|---|---|
| Ti6Al7Nb | 87.11 | 6.02 | 6.53 | 0.02 | 0.19 | 0.12 | 0.01 | - | - | - | - | - |
| YSZ | 0.02 | – | – | – | 0.01 | – | – | 68.03 | 4.29 | 2.04 | 0.01 | 25.6 |

which is in close range with that of the bone, in addition to excellent resistance to corrosion from the formation of passive titanium oxide layer ($TiO_2$) when it reacts with the body fluid [10]. However, this oxide and vanadium was recently discovered to be carcinogenic, according to the National Institute for Occupational Safety and Health and International Agency for Research on Cancer. To eliminate the deleterious effect of these substances, Ti6Al7Nb has recently gained attention, and it has proven to be an acceptable replacement for Ti6Al4V alloy [11]. Niobium, one of the major elements in the alloy, is non-toxic and does not adversely react with the human body. It also helps regulate the elastic modulus of the titanium alloy to a value closer to that of human bone.

Titanium exhibits a hexagonal close-packed structure (α-phase) at room temperature in its pure state. It undergoes an allotropic transformation at 882 $^{O}$C to a body-centred cubic structure (β-phase) [12,13]. The incorporation of stabilizing elements such as aluminium, vanadium and niobium results in the formation of crystalline α, β or α+β based on the respective phase stabilizer. Aluminium as an α-phase stabilizer increases the stabilizing temperature, while the β-phase is stabilized by niobium at a temperature below the transformation temperature, thereby forming a eutectoid system with titanium [14,15]. Yttria stabilized zirconia is formed from the stabilization of the cubic crystal structure of zirconium oxide ($ZrO_2$) with yttrium oxide ($Y_2O_3$) at room temperature. Amongst the commonly used ceramic reinforcement, YSZ has attracted the interest of several researchers in the field biomedical engineering for applications such as femoral ball, dental implants, ligaments, and prosthetic heart valves due to its low plaque affinity and high wear resistance [16,17]. Also, metallic based composites reinforced with YSZ has been proven to exhibit less susceptibility to leaching or corrosion, thereby eliminating the signs and symptoms of metal hypersensitivities in patients [18,19].

Recent research has shown the use of YSZ in dental fillings, implants, hip replacement, and femoral heads due to their osseointegration characteristics [20,21]. The mechanical properties of YSZ ceramic reinforcement include enhanced strength, toughness, and good transparency [22].

Corrosion is one of the major challenges that are faced by implants in humans, and this can be ascribed to the presence of proteins, water, dissolved oxygen, and ions such as hydroxides and chlorine in the body [23]. Dental implants face an aggressive environment in the mouth owing to the saliva's acidic pH, which ranges from 5.2 to 7.8 [24]. Furthermore, the effect of fluorine and hydrogen ions adversely affects the resistance of titanium alloys to corrosion, and this has been extensively studied [25,26]. Apart from the acidification induced by local foods and beverages, the promotion of an acidic environment by oral bacteria has been reported to be one of the main reasons for the decreased corrosion resistance of titanium and its alloys. This results in microbial corrosion immediately after the dental biomaterials are inserted into the mouth. The micro gaps between the abutments and implants, in addition to the surface of the outer implants, are covered by saliva and protein-rich pellicle fluid [27]. These liquids promote the transfer of bacteria to these implants.

Hanks' solution salt has been used by researchers in corrosion analysis of biocompatible materials for dental and orthopaedic applications as it provides an enabling environment that will maintain the physiological and structural integrity of human body fluid [28,29]. This special category of salt is designed to be used within a short term at ambient operating conditions. Aside its various classes of salt, it also contains glucose which is sterilized by membrane filtration [30]. Since the aim of this research is to ascertain the biocompatibility of the fabricated Ti6Al7Nb alloys, Hank's solution will therefore be used as the corrosive electrolyte.

**Table 2**
Composition based on mixing ratio of starting powders.

| Sample | Composition | Matrix: reinforcement ratio (%) |
|---|---|---|
| 1 | Ti6Al7Nb | 100:0 |
| 2 | Ti6Al7Nb + 1% YSZ | 99:1 |
| 3 | Ti6Al7Nb + 3% YSZ | 97:3 |
| 4 | Ti6Al7Nb + 5% YSZ | 95:5 |
| 5 | Ti6Al7Nb + 10% YSZ | 90:10 |

The nature of the passive oxide layer formed on the surface of the Ti6Al7Nb implant was investigated in Hank's solution by Lavos-Valereto and Wolynx [31]. The results from the study showed that the Ti6Al7Nb alloy formed a two-layer oxide film that comprised of a porous outer layer, and a dense inner layer. However, the excellent corrosion performance was ascribed to the former, while the latter layer enhanced the osseointegration capability. A more recent study by Hariharan et al. [32] determined the influence of yttria stabilized zirconia, and hydroxyapatite bioceramics on Ti6Al7Nb alloy. The bioceramics were deposited on the titanium alloy via electron beam coating technique. [33], as increased temperature during the coating process resulted in stoichiometric imbalance. The presence of the bioceramics further decreased the corrosion rate by 49.3%, and YSZ was specifically reported to aid bonding, thereby reducing the dissolution rate of the coated layer in the corrosive medium.

Owing to the establishment of the biocompatibility and enhanced mechanical properties of YSZ bioceramic and Ti6Al7Nb alloy, this present study investigates the effect of different volume percentage of YSZ bioceramics on the mechanical modification and corrosion behaviour of spark plamsa sintered Ti6Al7Nb-YSZ alloy in simulated body fluid (Hank's solution).

## 2. Experimental procedure

Ti6Al7Nb powder (particle size:20–63 μm) supplied by TLS Technik, Bitterfeld was used as the matrix, while Yttria (3 mol%) Stabilized Zirconia powder (particle size of D5Õ1 μm, Zr (Hf)O2:94,5% purity; $Y_2O_3$:5,2 ± 0,2%) supplied by Stanford Advanced Materials, USA served as the reinforcement. The elemental composition of the Ti6Al7Nb and YSZ starting powders are presented in Table 1. To ensure even distribution of the YSZ reinforcement within the Ti6Al7Nb matrix, the powders were mixed in a T2F Turbula shaker mixer for a period of 3 h at a speed of 49 rpm in a dry medium. The varying proportion of the dispersed YSZ reinforcement is presented in Table 2. The admixed powders were consolidated in a HHPD 25 Spark plasma sintering machine designed by FCT Germany. Prior to sintering, the admixed powders were poured into a graphite die coated with a graphite sheet. The latter ensured adequate conduction between the die and powder particles and also facilitated easy removal of the sintered specimens. The admixed powders and sintered compacts were further analysed using a Zeiss Sigma scanning electron microscope (SEM). X-ray diffraction (XRD) was carried out using a Rigaku Ultima IV diffractometer with monochromatic Kα and Cu radiation at 30 kV and 40 mA, while the present phases were identified using X'Pert Highscore software. The samples used for SEM and XRD analyses were sectioned to a dimension of 10 mm × 10 mm and prepared using standard metallographic

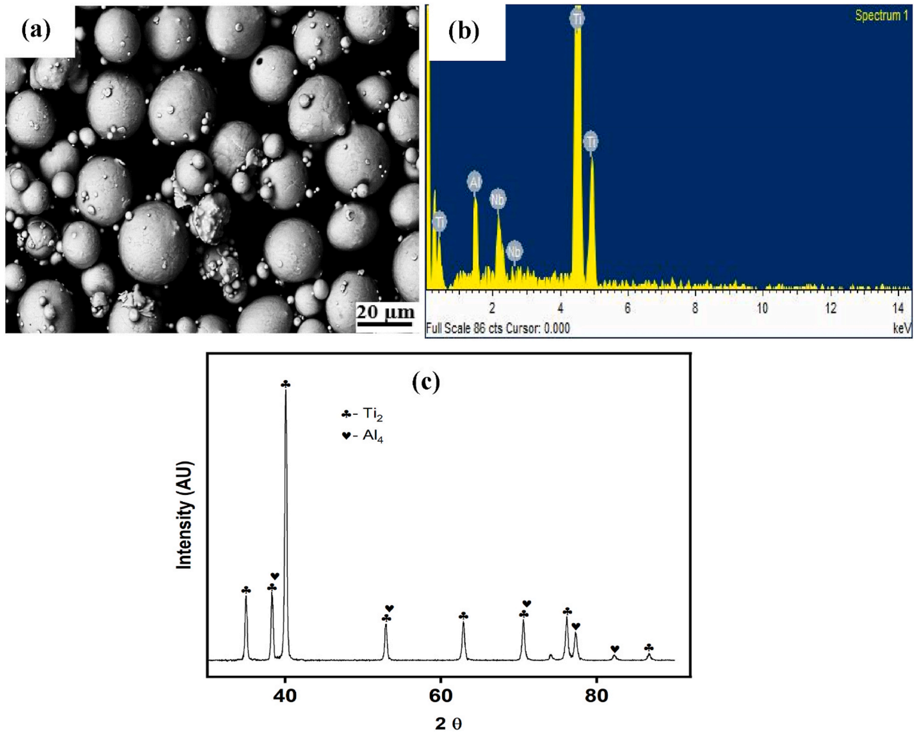


**Fig. 1.** (a) SEM (b) EDS and (c) XRD analysis of the Ti6Al7Nb powder.

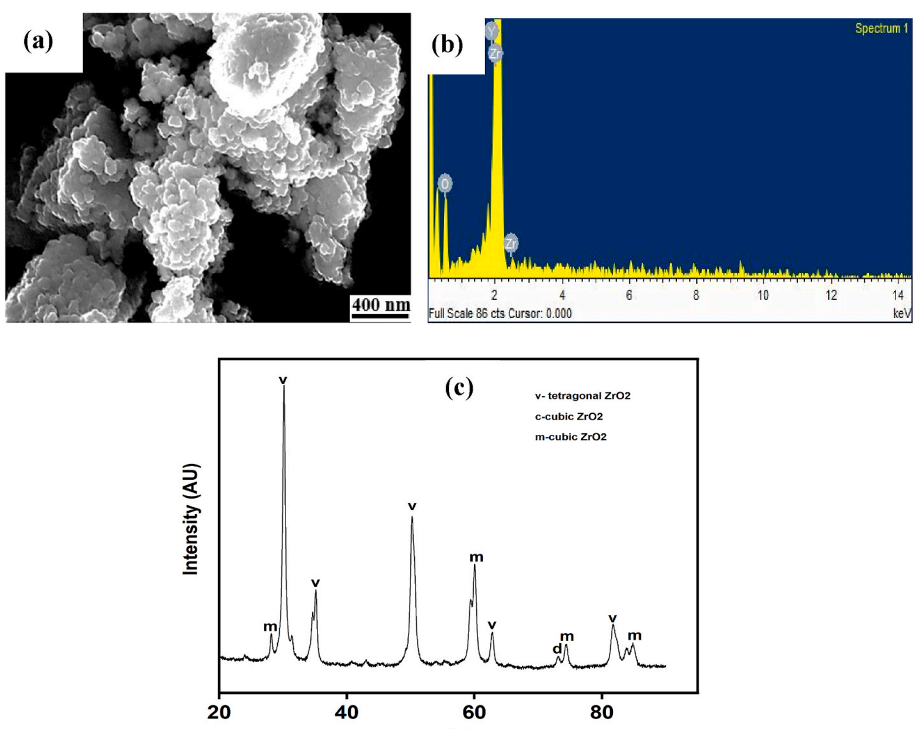


**Fig. 2.** (a) SEM (b) EDS and (c) XRD analysis of the YSZ powder.

procedures. Vickers hardness measurements were performed on a Falcon Innovatest hardness tester, and a load of 10 g was applied across the matrix and reinforcement phases. To assess the susceptibility of the specimens to biocorrosion in Hanks' Balanced Salt Solution (HBSS), electrochemical measurement was conducted using potentiodynamic polarization on a three-electrode VersaSTAT 4 potentiostat, which operates on a Versastudio software. The specimens were prepared for corrosion testing by attaching a conductive wire to one end of the specimen to ensure conduction, and this was followed by cold mounting in epoxy resin. To remove the resin layer formed on the surface of the specimen, it was further ground to 1000 grits of silicon carbide emery papers polished using diamond suspension to ensure a smooth surface. Open circuit measurements were conducted for 2 h prior to potentiodynamic polarization test to ensure the stability of the specimens in the

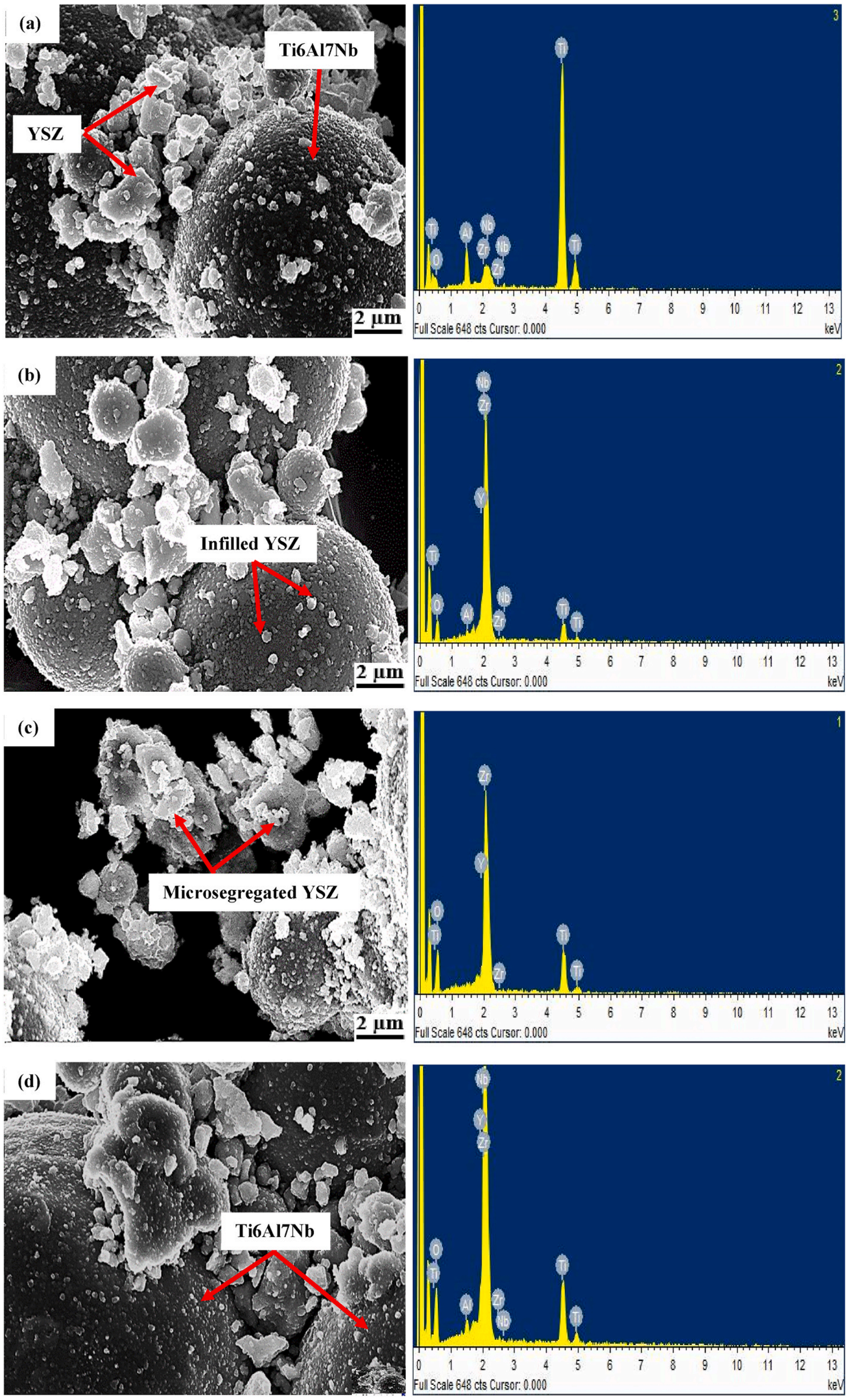


**Fig. 3.** SEM and EDS images of admixed Ti6Al7Nb and (a) 1% YSZ (b) 3% YSZ (c) 5% YSZ (d) 10% YSZ.

Hanks' solution. Potentidynamic polarization scans were carried out from an initial potential of −1.2 V to a final potential of 1.5 V at a scan rate of 0.2 mV/s. The tests were repeated severally for reproducibility. The SEM micrographs of the corroded surface were examined after the corrosion tests.

## 3. Results and discussion

### 3.1. Starting and admixed powders characterization

The SEM micrographs, EDS analysis in addition to the XRD phase analysis of the Ti6Al7Nb and YSZ powders are shown in Figs. 1 and 2 respectively. Fig. 1a presents a spherical morphology of the Ti6Al7Nb powder with few satellites that are tightly attached to the bigger satellites. The EDS analysis reveals the presence of titanium, aluminium and

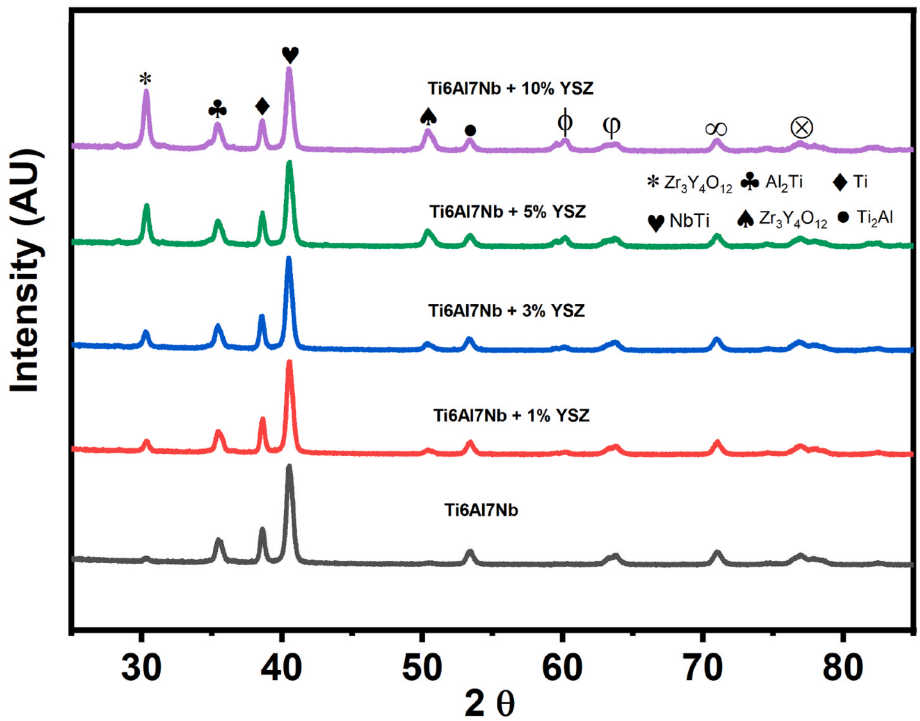


**Fig. 4.** XRD pattern of sintered compacts.

niobium as the principal elements present in the powder, with titanium exhibiting more dominance than aluminium and niobium. Fig. 1c shows the phases present in the powder. The peaks of both α and β phases are evident in the plot, and this confirms the stabilizing efficiency of aluminium and niobium. Likewise, the micrograph of YSZ, as seen in Fig. 2a reflects agglomerated powder particles. The EDS analysis shown in Fig. 2b agrees with the reported chemical composition, while the phase analysis (Fig. 2c) indicates the presence of monoclinic, tetragonal, and cubic $ZrO_2$ as the major phases in the powder. In powder metallurgy, powders are mixed to obtain an inter-particle dispersion, which ensures homogeneity between the powder constituents, although challenges such as varying particle size, shape and surface nature of individual powders have been identified. The influence of the mixer-induced force on the disintegration of the powder particles is shown in Fig. 3 (a–d). During mixing, the YSZ and Ti6Al7Nb powder particles are subjected to a drop and impact effect, which is supported by the mechanism of translation, inversion, and rotation motions [34]. The drop and impact force deforms the powders and reduces them to nano and submicron sizes. Fig. 3a and b shows the infilling of the YSZ particles into the Ti6Al7Nb micropores. Reduced particles of the YSZ diffuse into the micropores formed from the defragmentation of the Ti6Al7Nb owing to the shear force from the mixer. Moreover, Fig. 3c and d reveal minimal segregation and agglomeration in the admixed powders. It is noteworthy that segregation often occurs when there is a difference between the particle sizes and structural morphology of the powders to be mixed [35]. However, recent mixing equipment is designed to reduce this challenge.

### 3.2. Phase identification and microstructural analyses

The XRD patterns exhibited by the sintered compacts are studied to understand possible chemical reactions and phase transformations that occurred owing to the mixing and spark plasma sintering technique adopted for the consolidation of the powders. The plot of the patterns generated from the XRD analysis is presented in Fig. 4. The strongest peaks are seen to be recorded at 2 θ values of 30.33°, 35.44°, 38.59°, 40.32°, 40.48°, 50.30° and 53.32°. The analysis further shows that only α and β Ti phases are dominant in the unreinforced Ti6Al7Nb specimen. This behaviour can be attributed to the presence of Al and Nb, which act as phase stabilizers. The broadening of peak observed in the peak formed at a 2 θ value of 30.33° with an increase in the volume percentage of the YSZ reinforcement also indicates a decrease in crystallite size of the Ti6Al7Nb composites. The broadening evident in other peaks can be as a result of reduced structural deformation from the mixing technique used for dispersion of the reinforcement within the matrix [8]. It is noteworthy that the spark plasma sintering (SPS) method does not promote even solidification of admixed powders in a liquid state; hence, a solid-state reaction occurs between the Ti6Al7Nb and YSZ, which supports the formation of YSZ precipitates around the boundary of Ti6Al7Nb matrix [36].

The microstructural evolution of the Ti6Al7Nb matrix and composites reinforced with YSZ is investigated under an optical microscope, and the micrographs obtained are presented in Fig. 5. Fig. 5a shows the distribution of acicular and globular α (white) grains within the β grains (dark). The acicular α phase exhibits a basketweave arrangement, which is also an attribute of the Widmanstätten structure. A similar microstructure was reported in a study by Bolzoni et al. [37]. The incorporation of 1 and 3% YSZ reinforcements as revealed in Fig. 5b and c led to a more homogeneous microstructure with the combination of α grains and evenly distributed α+β lamellae across the micrographs, and this behaviour can be ascribed to the homogeneous distribution of these reinforcement particles, even though the presence of some undissolved reinforcements is evident. Fig. 5d and e, which presents the micrographs of composites with increased YSZ addition (5% and 10%), further reveal microconstituent coarsening, which increases the grain size of the Ti6Al7Nb matrix. A higher reinforcement proportion and sufficient holding time during sintering can promote the formation of coarse β grains and increase the size of the α grains. It should be noted that there is nucleation of the α grains nucleated from the β grains when the sintering temperature is between 1200 and 1350 °C [38]. The absence of pores in the microstructure can also be attributed to adequate mixing of the matrix and reinforcement. The SEM morphology of the sintered specimens is seen in Fig. 5(a–e). As revealed in Fig. 6a, the Ti6Al7Nb shows a two-phase microstructure with increased grains. The distance

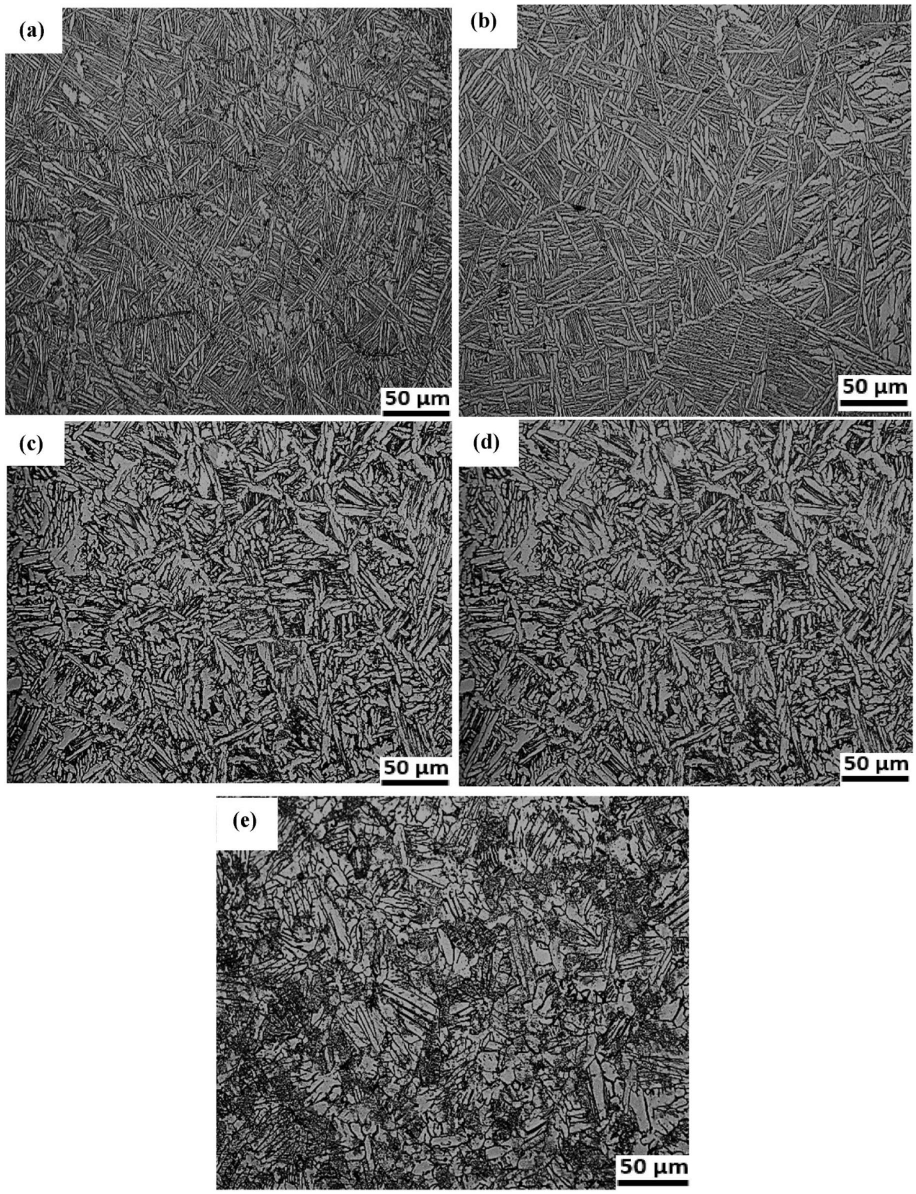


**Fig. 5.** Optical micrographs of spark plasma sintered (a) Ti6Al7Nb (b) Ti6Al7Nb + 1%YSZ (c) Ti6Al7Nb + 3%YSZ (d) Ti6Al7Nb + 5%YSZ (e) Ti6Al7Nb + 10%YSZ.

between the basketweave laths is quite irregular in comparison with the microstructures of the reinforced Ti6Al7Nb specimens. This can be due to the body centre cubic (bcc) crystal structure of the β-Ti, which has a smaller atomic packing factor than the α-Ti with a hexagonal closed pack structure (hcp). Fig. 6b presents slight/no microstructural variation due to the reduced proportion of the YSZ particles Fig. 6c confirms even dispersion of the YSZ particles across the boundaries of the Ti6Al7Nb matrix. Comparing this with the previously discussed micrograph, the microstructure is seen to be refined, with the formation of more phases upon the addition of YSZ reinforcement. Fig. 6d and e shows larger and well-dispersed reinforcements with a bit of agglomeration evident in Fig. 6d. The increased YSZ addition is also seen to promote grain size refinement, and the lamellar spacing between the α and β colonies becomes smaller. The addition of the YSZ particles provides sites for nucleation and increases the amount of energy stored. A similar observation was reported in a study by Singh et al. [39]. It is also important to note that excessive addition of reinforcement causes movement of a valence electron, which increases interatomic bonding due to its low ionization energy and the extra stress field, which prevents atomic diffusion of the reinforcement particles [40]. Therefore, the proportion of incorporated reinforcement into the matrix system should be minimal.

### 3.3. Microhardness

The values obtained from the measurement of Vickers microhardness of the unreinforced Ti6Al7Nb alloy and YSZ reinforced alloys are illustrated in Fig. 7. The unreinforced Ti6Al7Nb alloy records the least microhardness value of 302.5 HV, and this value is seen to undergo a spontaneous increase upon an increase in the proportion of incorporated YSZ reinforcement. The fatigue life and wear properties of Ti6Al7Nb alloys are improved when the hardness property is sufficiently enhanced, thereby reducing the need for revision surgeries [41]. From Fig. 7, the increased hardness values of the reinforced Ti6Al7Nb alloys can be related to solid solution strengthening, which results from elastic interactions between the solute and dislocation strain fields [42]. The incorporated YSZ atoms stir up strengthening by solid solution mechanism regardless of the diffusional transformation of the α phase to β phase at high temperature. Furthermore, the reduced particle size of the YSZ reinforcement played a crucial role in improving the hardness

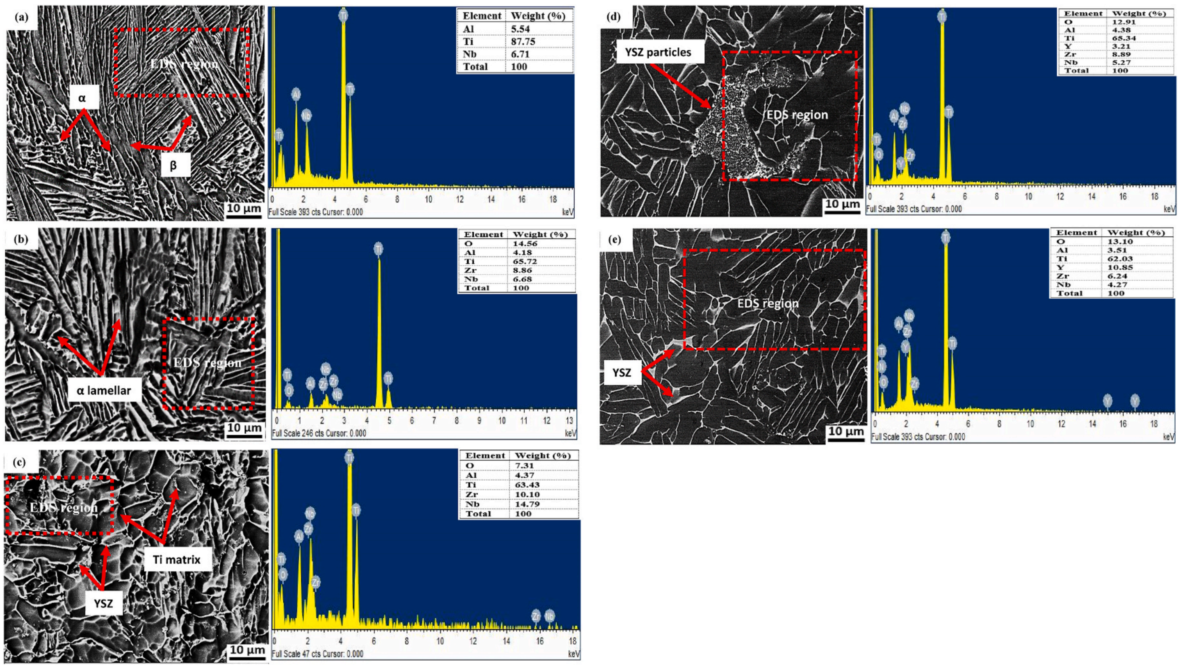


**Fig. 6.** SEM micrographs of sintered (a)Ti6Al7Nb (b) Ti6Al7Nb + 1%YSZ (c) Ti6Al7Nb + 3%YSZ (d) Ti6Al7Nb + 5%YSZ (e) Ti6Al7Nb + 10%YSZ.

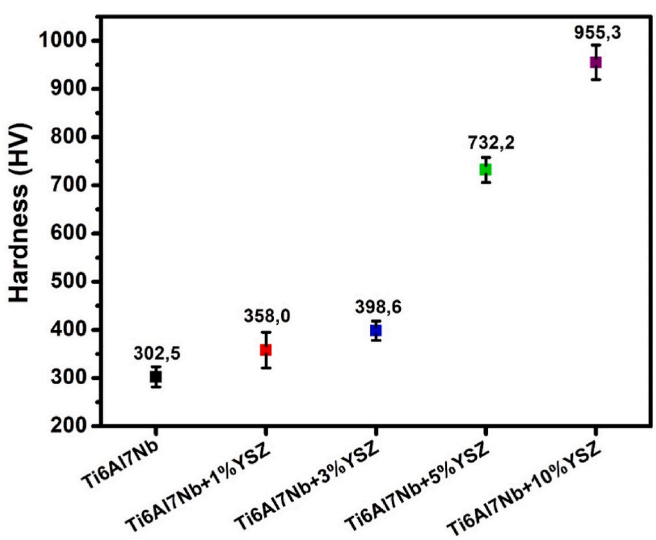


**Fig. 7.** Plot of hardness values with error bars for sintered compacts.

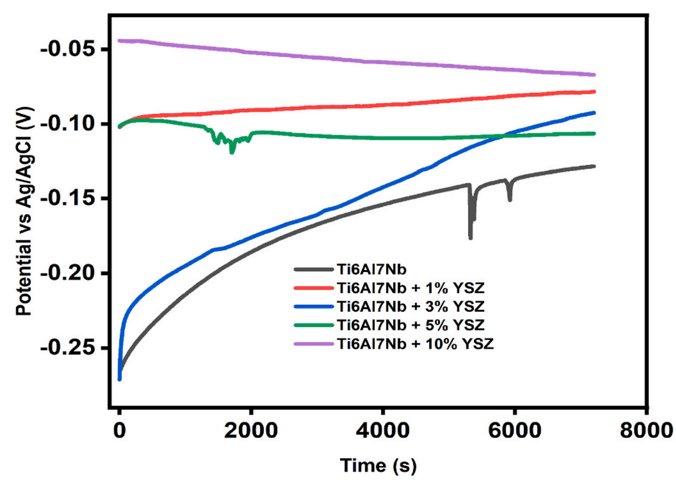


**Fig. 8.** Open circuit potential plots for sintered specimens in Hanks' solution.

property of the composites. Research has shown that nanosized particles often exhibit an excellent sintering rate owing to their high driving force and short migration distance. These particles also promote uniform distribution, enhancing high density and homogeneous structure [43]. Also, the change in particle and shape during powder mixing can induce a strengthening effect through grain refinement, increasing the composites' hardness property. Other mechanisms contributing to hardness enhancement in titanium composites include the Friedel-Fleisher effect, Orowan strengthening and the Hall-Petch effect [44]. The former can account for the strengthening effect induced by substitutional YSZ atoms in the Ti6Al7Nb lattice [45]. The formation of precipitates owing to the addition of reinforcements to the Ti6Al7Nb alloy occurs in a discontinuous trend and is dependent on time and temperature. This subject the constituents of the composites to irregular distribution, which accumulate in the lattice at high temperature, leading to clustering or local superstructure such as one phase separation. Guinier-Preston (GP) zones are formed at sufficient time and temperature in the solid solution, and this makes them exhibit a strengthening effect similar to coherent precipitations. If the precipitated particles are large and hard (YSZ), dislocation line begins to bend within the region of the particle in accordance with Orowan mechanism until it is enclosed, and bow out leaving a loop around the particles [46]. According to a study by Jiang et al. [47]. There can be a possible formation of $AlZr_3$ compound, which often act as a strengthening phase in composite/alloy systems. However, further increment in the proportion of YSZ reinforcement will not produce any significant change in the microstructural evolution but can promote the formation of more dominant YSZ phases which can enhance the mechanical properties of the composites.

### *3.4. Corrosion study in Hanks' solution*

The response to the sintered compacts to biocorrosion was analysed in Hanks' solution using open circuit and potentiodynamic polarization electrochemical techniques, and the plots obtained are presented in

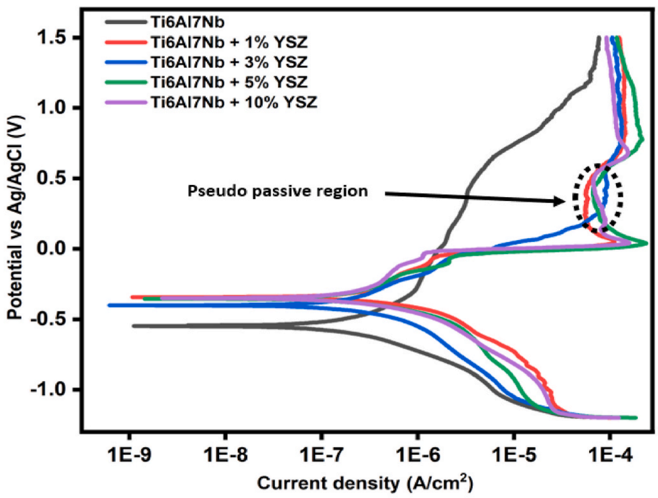


**Fig. 9.** Potentiodynamic polarization curves of sintered samples in Hanks' solution.

**Table 3**
Corrosion parameters of the sintered specimens from Tafel extrapolation.

| Specimen | Ecorr (mV) | Icorr (nA) | Anodic current (mV) | Cathodic current (mV) |
|---|---|---|---|---|
| Ti6Al7Nb | −433.40 | 551.75 | 535.66 | 535.66 |
| Ti6Al7Nb+1% YSZ | −245.83 | 565.43 | 389.18 | 389.18 |
| Ti6Al7Nb+3% YSZ | −383.02 | 541.60 | 506.65 | 506.65 |
| Ti6Al7Nb+5% YSZ | −309.64 | 937.21 | 517.81 | 517.81 |
| Ti6Al7Nb+10% YSZ | −151.87 | 665.93 | 556.13 | 556.13 |

Figs. 8 and 9, respectively. To support the potentiodynamic polarization plot, the curves were fitted using Tafel extrapolation on the Versastudio software, and the relevant corrosion parameters obtained are recorded in Table 3. Open circuit potential provides information on the passive or active state of a material, as well as critical information on the oxide layer's stability in passive materials such as titanium. From Fig. 8, the unreinforced Ti6Al7Nb specimen and alloy with 3% YSZ are seen to undergo a sporadic potential increase by shifting to a more noble direction, thereby indicating the formation of stable oxide layers on the surface of the specimens with time. Lakshmi et al. [48] reported a similar observation in their study. However, other specimens showed higher corrosion potential with a bit of fluctuation seen in the specimen reinforced with 5% YSZ. This fluctuation seen in the plots can be ascribed to the dissolution and rapid formation of passive film on the surface of the specimens. Overall, the specimen with 10% YSZ exhibited more resistance to dissolution in the test electrolyte, while the unreinforced sintered Ti6Al7Nb alloy showed the least stability in the solution. It is noteworthy that the shift in the potential of the reinforced Ti6Al7Nb alloys towards the electropositive direction, does not depict corrosion enhancement, but it shows that the reinforced alloys are thermodynamically stable in the Hanks' solution. The potentiodynamic polarization curves is represented in Fig. 9. The specimens show different curves, with the unreinforced Ti6Al7Nb exhibiting the least corrosion resistance as it records a corrosion potential and current density of −0.43 V and 551.75 nA, respectively. Additionally, the incorporation of YSZ particles into the Ti6Al7Nb matrix increased the corrosion resistance of the resulting composites as the corrosion potential shifted towards the electropositive direction. However, the composite with 3% YSZ displayed the highest susceptibility to corrosion as it records a corrosion potential of −0.38 V. In comparison, the least corrosion susceptibility is evident in the specimen reinforced with 10% YSZ as its corrosion potential shifts more towards the electropositive direction with a corrosion potential of −0.15 V. This behaviour can also be a result of the formation of higher quantity of cathodic β-phase, which prevented the corrosion of the α-YSZ phases. Further observation also reveals that all the sintered compacts have similar current density, which indicates they have close oxide layers in the electrolyte. It is also important to note that the unreinforced Ti6Al7Nb specimen shows a bit of passivity, while the composites exhibit a pseudopassivity as seen in the circled region in Fig. 8 Between the potential range of 0.1 V and 0.6 V due to dissolution and regeneration of protective layers on the surface of the specimens during the corrosion test. Porcayo-Palafox et al. [49] reported a similar observation in their study, as all the investigated biomaterials exhibited both passive and pseudopassive behaviour.

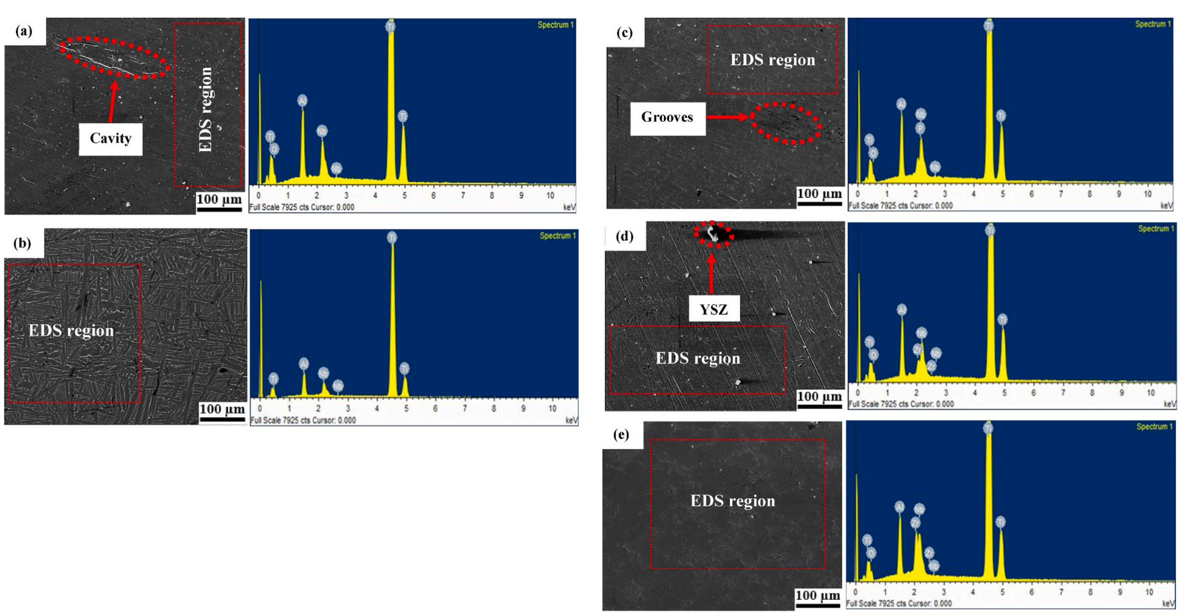


**Fig. 10.** Post corosion SEM examination of sintered (a) Ti6Al7Nb ((b) Ti6Al7Nb + 1%YSZ (c) Ti6Al7Nb + 3%YSZ (d) Ti6Al7Nb + 5%YSZ (e) Ti6Al7Nb + 10%YSZ.

### 3.5. Post-corrosion surface examination

Fig. 10 reveals the morphology of the sintered specimens after the potentiodynamic polarization test in Hanks' solution as analysed by SEM. The respective EDS spectrum taken across each micrograph is attached to the SEM images to provide information on the elements retained on the specimen surface after corrosion. The EDS images of the composites are seen to contain dominant titanium, niobium, aluminium and zirconium and oxygen peaks. Generally, titanium and its alloys are prone to aggressive corrosive attack since they have the ability to form passive oxide layers, which isolate them from corrosive environment. From Fig. 10a, a deep cavity is generated on the surface of the sample, owing to the attack of corrosive ions present in the Hanks' electrolyte. The micrograph presented in Fig. 10b shows a different phenomenon, as the presence of large cavity is absent. Instead, localized corrosion across the surface of the specimen the evident. The Ti6Al7Nb matrix suffers from anodic corrosion due to several microscopic corrosion cells forming between the matrix sites and the phases formed by the reinforcement particles (cathode). However, an increase in the proportion of the incorporated reinforcement in Fig. 10c revealed a surface with a grooves pattern, and this shows that the formation and growth of passive oxide layers is evident in the specimen [50]. Further increase in the volume percentage of the YSZ particles to 5% in Fig. 10d shows an inhomogeneous surface characterized by the formation of ridges. This is related to its higher corrosion potential value and the evident pseudo-passive behaviour it exhibits. However, the evidence of pitting or localized corrosion is rarely observed in Fig. 10e, owing to the high proportion of YSZ particles incorporated into the alloy matrix. This indicates that YSZ reinforcement provided adequate protection to the Ti6Al7Nb substrate. One of the reasons for the superior hard-tissue compatibility of titanium and its alloy over other metals is its self-capacity to generate biocompatible calcium phosphate [51], and this feature is often used to increase the hard-tissue compatibility of titanium and its alloys through surface modification. Moreover, YSZ has been reported to generate zirconium phosphate in Hanks' solution, which has is also a biocompatible compound [52,53].

## 4. Conclusion

In this study the microstructural characteristics, microhardness and biocorrosion behaviour of

Ti6Al7Nb samples without and with addition of yttria stabilized zirconia fabricated by spark

Plasma sintering technique have been investigated, and the conclusions are as follow:

- The Ti6Al7Nb depicts an α/β structure with the distribution of acicular and globular α (white) grains within the β grains (dark). The addition of 1, 3, 5 and 10 wt% YSZ reinforcements show a more homogeneous microstructure with the presence of α grains and evenly distributed α+β lamellae.
- Increasing the yttria stabilized zirconia content in Ti6Al7Nb alloy from 1 to 10 wt % increases the vickers microhardness and biocorrosion resistance of the alloy.
- Ti6Al7Nb + YSZ composites show a significant noble shift in $E_{corr}$ and lower corrosion current density ($I_{corr}$).
- The incorporation of YSZ enhanced the formation of oxide passive layers, which promoted the corrosion resistance of the reinforced YSZ composites. This was further confirmed by the presence of oxygen in the EDS spectrum analysed by SEM.

## CRediT authorship contribution statement

**Nondumiso Prudence Msweli:** Experimentation, Data curation, Methodology, Formal analysis. **Samuel Olukayode Akinwamide:** Conceptualization, Formal analysis, writing of original draft, Visualization, Supervision. **Peter Apata Olubambi:** Conceptualization, Review and editing, Project administration, Supervision. **Babatunde Abiodun Obadele:** Conceptualization, experimentation, Resources, Supervision, Funding acquisition.

## Declaration of competing interest

The authors declare that they have no known competing financial interests or personal relationships that could have appeared to influence the work reported in this paper.

## Data availability

Data will be made available on request.

## Acknowledgement

The authors are grateful to National Research Foundation (NRF), South Africa for financial support under the.Thuthuka Grant number TTK180419322687 UID: 117843.

## References

[1] A.R. Memon, et al., A review on computer-aided design and manufacturing of patient-specific maxillofacial implants, Expet Rev. Med. Dev. 17 (4) (2020) 345–356.

[2] S. Şahin, M.C. Cehreli, E. Yalçın, The influence of functional forces on the biomechanics of implant-supported prostheses—a review, J. Dent. 30 (7–8) (2002) 271–282.

[3] M. Semlitsch, H. Willert, Properties of implant alloys for artificial hip joints, Med. Biol. Eng. Comput. 18 (4) (1980) 511–520.

[4] J.T. Steigenga, et al., Dental implant design and its relationship to long-term implant success, Implant Dent. 12 (4) (2003) 306–317.

[5] C.A. Bain, P.K. Moy, The association between the failure of dental implants and cigarette smoking, Int. J. Oral Maxillofac. Implants 8 (6) (1993).

[6] K. Yang, Y. Ren, Nickel-free austenitic stainless steels for medical applications, Sci. Technol. Adv. Mater. 11 (2010), 014105.

[7] H.-Y. Lin, J.D. Bumgardner, Changes in the surface oxide composition of Co–Cr–Mo implant alloy by macrophage cells and their released reactive chemical species, Biomaterials 25 (7–8) (2004) 1233–1238.

[8] T.S. Tshephe, et al., Structural characterization and biocorrosion behaviour of direct metal laser sintered Ti6Al4V–ZrO2 tracks: influence of processing parameters, Results in Materials 13 (2022), 100257.

[9] B.A. Obadele, et al., Improving the tribocorrosion resistance of Ti6Al4V surface by laser surface cladding with TiNiZrO2 composite coating, Appl. Surf. Sci. 345 (2015) 99–108.

[10] S. Liang, Review of the design of titanium alloys with low elastic modulus as implant materials, Adv. Eng. Mater. 22 (11) (2020), 2000555.

[11] T.S. Tshephe, et al., Additive manufacturing of titanium-based alloys- A review of methods, properties, challenges, and prospects, Heliyon 8 (3) (2022), e09041.

[12] K. Edalati, et al., High-pressure torsion of titanium at cryogenic and room temperatures: grain size effect on allotropic phase transformations, Acta Mater. 68 (2014) 207–213.

[13] O.J. Akinribide, et al., The role of graphite addition on spark plasma sintered titanium nitride, J. Mater. Res. Technol. 9 (3) (2020) 6268–6277.

[14] I. Hulka, et al., Mechanical properties and corrosion behavior of thermally treated Ti-6Al-7Nb dental alloy, Materials 15 (11) (2022) 3813.

[15] G.N. Mekgwe, et al., Fabrication of graphite reinforced TiCxNy by spark plasma sintering technique: a comparative assessment of microstructural integrity and nanoindentation properties, Vacuum 187 (2021), 110144.

[16] M. Taheri, et al., Mechanical properties of 3Y-TZP/CNTs composites, Ceram. Int. 40 (2) (2014) 3347–3352.

[17] M. Kovochich, et al., Understanding outcomes and toxicological aspects of second generation metal-on-metal hip implants: a state-of-the-art review, Crit. Rev. Toxicol. 48 (10) (2018) 839–887.

[18] J.G. Thakare, R.S. Mulik, M.M. Mahapatra, Effect of carbon nanotubes and aluminum oxide on the properties of a plasma sprayed thermal barrier coating, Ceram. Int. 44 (1) (2018) 438–451.

[19] T. Arunkumar, et al., Effect of multiwalled carbon nanotubes on improvement of fracture toughness of spark-plasma-sintered yttria-stabilized zirconia nanocomposites, J. Mater. Eng. Perform. 30 (6) (2021) 3925–3933.

[20] A. Beketova, et al., Sol–gel synthesis and characterization of YSZ nanofillers for dental cements at different temperatures, Dent. J. 9 (11) (2021) 128.

[21] G. Ayoub, et al., Composite nanostructured hydroxyapatite/yttrium stabilized zirconia dental inserts–The processing and application as dentin substitutes, Ceram. Int. 44 (15) (2018) 18200–18208.

[22] G. Dercz, et al., Characterization of YSZ coatings deposited on cp-Ti using the PS-PVD method for medical applications, Coatings 11 (11) (2021) 1348.

[23] D.S. Fisher, et al., Plasma, oral fluid, and whole-blood distribution of antipsychotics and metabolites in clinical samples, Ther. Drug Monit. 35 (3) (2013) 345–351.
[24] G. Manivasagam, D. Dhinasekaran, A. Rajamanickam, Biomedical implants: corrosion and its prevention-a review, Recent Pat. Corros. Sci. 2 (1) (2010).
[25] B.M. Fraser, Does fluoride cause corrosion of titanium dental implants, Int. J. Oral Implant. Clin. Res. 9 (2018) 7–10.
[26] Z. Wang, et al., Comparison of the corrosion behavior of pure titanium and its alloys in fluoride-containing sulfuric acid, Corrosion Sci. 103 (2016) 50–65.
[27] B.E. Nagay, J.M. Cordeiro, V.A. Barao, Insight into corrosion of dental implants: from biochemical mechanisms to designing corrosion-resistant materials, Curr. Oral Health Rep. (2022) 1–15.
[28] J. Niu, et al., Improved mechanical, bio-corrosion properties and in vitro cell responses of Ti-Fe alloys as candidate dental implants, Mater. Sci. Eng. C 122 (2021), 111917.
[29] S. Prithivirajan, et al., Bio-corrosion impacts on mechanical integrity of ZM21 Mg for orthopaedic implant application processed by equal channel angular pressing, J. Mater. Sci. Mater. Med. 32 (6) (2021) 1–13.
[30] A. Fattah-alhosseini, M. Pourmahmoud, Passive and semiconducting properties assessment of commercially pure tantalum in Hank's physiological solution, J. Mater. Eng. Perform. 27 (1) (2018) 116–123.
[31] I.C. Lavos-Valereto, et al., Electrochemical impedance spectroscopy characterization of passive film formed on implant Ti–6Al–7Nb alloy in Hank's solution, J. Mater. Sci. Mater. Med. 15 (1) (2004) 55–59.
[32] K. Hariharan, et al., Experimental investigation of bioceramic (Hydroxyapatite and Yttrium stabilized zirconia) composite on Ti6Al7Nb alloy for medical implants, Mater. Manuf. Process. 35 (5) (2020) 521–530.
[33] H. Chouirfa, et al., Review of titanium surface modification techniques and coatings for antibacterial applications, Acta Biomater. 83 (2019) 37–54.
[34] M. Poux, et al., Powder mixing: some practical rules applied to agitated systems, Powder Technol. 68 (3) (1991) 213–234.
[35] B.A. Obadele, Z.H. Masuku, P.A. Olubambi, Turbula mixing characteristics of carbide powders and its influence on laser processing of stainless steel composite coatings, Powder Technol. 230 (2012) 169–182.
[36] P. Nandwana, et al., Formation of equiaxed alpha and titanium nitride precipitates in spark plasma sintered TiB/Ti–6Al–4V composites, Mater. Lett. 83 (2012) 202–205.
[37] L. Bolzoni, E.M. Ruiz-Navas, E. Gordo, Evaluation of the mechanical properties of powder metallurgy Ti-6Al-7Nb alloy, J. Mech. Behav. Biomed. Mater. 67 (2017) 110–116.
[38] W. Cui, et al., High temperature deformation behavior of α+ β-type biomedical titanium alloy Ti–6Al–7Nb, Mater. Sci. Eng. 499 (1–2) (2009) 252–256.
[39] N. Singh, et al., Effect of TiB2 addition on the mechanical and biological response of spark plasma sintered Ti6Al7Nb matrix composites, J. Alloys Compd. 924 (2022), 166502.
[40] Y. Feng, et al., Effect of LaB6 addition on the microstructure and properties of (Ti3Al+ TiB)/Ti composites by laser cladding, Mater. Des. 181 (2019), 107959.
[41] X. Shen, et al., Improvement in mechanical properties of titanium alloy (Ti-6Al-7Nb) subject to multiple laser shock peening, Surf. Coating. Technol. 327 (2017) 101–109.
[42] R.L. Fleischer, Substitutional solution hardening, Acta Metall. 11 (3) (1963) 203–209.
[43] Y. Liu, et al., Inhibited grain growth in hydroxyapatite–graphene nanocomposites during high temperature treatment and their enhanced mechanical properties, Ceram. Int. 42 (9) (2016) 11248–11255.
[44] Z. Zhou, et al., Microstructure evolution and mechanical properties of in-situ Ti6Al4V–TiB composites manufactured by selective laser melting, Compos. B Eng. 207 (2021), 108567.
[45] B.M. Moshtaghioun, et al., Titanium carbonitride fabricated by spark plasma sintering: is it a ceramic model of carbon-induced Friedel-Fleisher strengthening effect? J. Eur. Ceram. Soc. 41 (13) (2021) 6275–6280.
[46] C.J. Zhang, et al., A titanium composite with dual reinforcements of micrometer sized TiB and submicrometer sized Y2O3, Mater. Lett. 233 (2018) 242–245.
[47] X.J. Jiang, et al., Microstructure and mechanical properties of ZrAl binary alloys, J. Alloys Compd. 811 (2019), 152068.
[48] S.G. Lakshmi, et al., In vitro corrosion behaviour of plasma nitrided Ti–6Al–7Nb orthopaedic alloy in Hanks solution, Sci. Technol. Adv. Mater. 4 (5) (2003) 415.
[49] E. Porcayo-Palafox, et al., Electrochemical performance of Ti-based commercial biomaterials, Adv. Mater. Sci. Eng. 2019 (2019), 4352360.
[50] D. Kuczyńska-Zemła, et al., Corrosion behavior of titanium modified by direct laser interference lithography, Surf. Coating. Technol. 418 (2021), 127219.
[51] R. Kumari, J.D. Majumdar, Studies on corrosion resistance and bio-activity of plasma spray deposited hydroxylapatite (HA) based TiO2 and ZrO2 dispersed composite coatings on titanium alloy (Ti-6Al-4V) and the same after post spray heat treatment, Appl. Surf. Sci. 420 (2017) 935–943.
[52] M. Oishi, et al., Surface changes of yttria-stabilized zirconia in water and Hanks solution characterized using XPS, Surf. Interface Anal. 50 (5) (2018) 587–591.
[53] M. Oishi, et al., Surface characterization of commercially available yttria-stabilized tetragonal zirconia polycrystalline in water and Hanks' solution using X-ray photoelectron spectroscopy, Dent. Mater. J. 38 (3) (2019) 496–504.